Instruments and Methods

Measurement of strain-rate components in a glacier with embedded inclinometers

Arne KELLER,[1] Heinz BLATTER[2]

[1] *Versuchsanstalt für Wasserbau, Hydrologie und Glaziologie (VAW), ETH Zürich, Zürich, Switzerland*
E-mail: keller@vaw.baug.ethz.ch
[2] *Institute for Atmospheric and Climate Science, ETH Zürich, Zürich, Switzerland*

ABSTRACT. We present measurements with inclinometer/magnetometer probes inserted in glacier ice, and discuss the underlying mathematical theory to extract velocity-gradient components from these data. Assumptions concerning the ice flow field must be made to reduce the number of unknowns and to close the system of equations obtained from the theory. With the incompressibility assumption and the first-order plane-strain approximation, the evolution equation for the tilt of the main sensor axis can be solved exactly and the obtained function can be fitted to measured data to obtain optimal shear and normal strain components. Daily variations superposed on the tilt evolution reflect variations in sliding and perhaps partial elastic recovery of deformations.

INTRODUCTION

Due to the limited accessibility of the subglacial and englacial environment, the determination of subsurface ice velocities and components of the strain rate and stress is a technically difficult and expensive task. Such information is of crucial importance for understanding basal processes, such as variable basal sliding and its consequences for the near-basal strain field.

A number of methods and techniques, mostly in boreholes, have been applied to probe the englacial velocity and strain fields. An often used method is the observation of ice deformation in an open borehole with inclinometry (Gerrard and others, 1952; Sharp, 1953; Raymond, 1971; Hooke and Hanson, 1986; Hooke and others, 1992). This method was used to determine longitudinal strain in a chain of boreholes (Shreve and Sharp, 1970), to identify extrusion flow type velocity profiles (Hooke and others, 1987), to determine local sliding velocities (Copland and others, 1997) and to investigate the effect of a cold margin on ice flow (Moore and others, 2011). Harper and others (1998, 2001) used arrays of boreholes to determine three-dimensional flow and strain fields. Various methods were applied to measure vertical strain rates in open boreholes (Paterson, 1976; Raymond and others, 1994; Gudmundsson, 2002; Hawley and others, 2002; Sugiyama and Gudmundsson, 2003). Schwerzmann and others (2006) used a combined inclinometer/caliper probe to measure the velocity profile together with the closure, cross-sectional deformation and vertical normal strain of a borehole.

The installation of continuously measuring inclinometers in boreholes allows us to perform measurements of high temporal resolution (Gudmundsson and others, 1999; Amundson and others, 2006). This method continuously observes the tilt and azimuth of the axes of instruments that are inserted into the ice. Modeled tilt curves that are calculated from assumed or modeled flow fields were fitted to the measured tilt curves to interpret the measurements.

An in situ measurement of the stress–strain-rate relation of glacier ice can only be performed if all stress components and strain components are measured simultaneously at the same location within the ice (Pfeffer and others, 2000; Marshall and others, 2002) without additional assumptions on the flow field or numerical modeling. In this work we propose and discuss a technique that allows us to meet these requirements for measurements of strain rates. The practical application of this technique may not be trivial, and in fact, the analysis was carried out as a result of difficulties in an experiment on Rhonegletscher, Switzerland. The coupling of the instruments to the ice in boreholes in temperate ice may take several months and seems to be unstable even then.

For the evaluation of the inclinometer data we assume that the instrument behaves as a Lagrangian unit vector attached to the ice, which leads to a time-evolution equation for the unit vector. This equation is (to lowest order in the time-step) identical to the one Gudmundsson and others (1999) solved by an explicit Euler method. The evolution equation for the unit vector can be solved analytically with two restrictive assumptions: (1) the flow field is well represented with the plane-strain first-order approximation (Blatter, 1995) and (2) the strain components are constant over the measurement period.

In the following sections, we give some technical information on the inclinometer/magnetometer probes and their calibration. The mathematical theory of strain measurements with inclinometer probes is outlined and discussed, and we present an analysis of time series of zenith and azimuth angles of probe axes to determine the strain components if only one sensor is available and show some examples of time series observed in Alpine glaciers. In the final section (Conclusions and prospects), we discuss the possibilities for strain measurements and propose experiments to further develop the method.

INCLINOMETER PROBE

The inclinometer probe consists of a cylindrical aluminum casing of 46 mm diameter and 63 mm length. A two-axis inclinometer of type SCA100T-D01 (VTI Technologies,

https://doi.org/10.3189/2012JoG11J234 Published online by Cambridge University Press

http://www.vti.fi/en/products/inclinometers) with a nominal resolution of 0.044 mrad, and a three-axis magnetometer of type MicroMag3 (PNI Corporation, http://www.pnicorp.com/products/products) with a nominal resolution of 0.015 μT allow us to measure the absolute direction of the probe axis in space and, furthermore, to determine the absolute orientation of an orthogonal set of vectors that are fixed with respect to the casing. The limiting factor for the accuracy is given by the magnetometers and the large uncertainty in the orientation of the Earth's magnetic field at depth in the ice.

Calibration and processing of data

The combined inclinometer/magnetometer probes provide the strength of the magnetic field along three axes and the strength of the gravity field along two axes,

$$S_i = a_i R_i + b_i, \quad i = 1, \ldots, 5 \tag{1}$$

where R_i are the magnetic and gravity field strengths, S_i are the readings of the sensor output, a_i are the slopes of linear functions and b_i are the offsets at zero field strength. The ten unknown parameters, a_i and b_i, must be determined by a calibration procedure.

Ideally, the calibration should be performed under laboratory conditions. If, however, the absolute value and the orientation of the magnetic field at the site of the measurement is not known, the problem can still be treated with the same number of unknown parameters. In this case, we simply assume the R_i to be normalized fields, and the parameters depend on the absolute field strengths. For the magnetic field this means that the calibration has to be repeated on site, as the geomagnetic field there may be different from that in the laboratory.

Given a parameterization of the pure rotations in three dimensions, three parameters completely describe the orientation of the instrument with respect to a fixed coordinate system at a given measurement. For N measurements, there are $3N$ unknown orientation parameters, i.e. a total of $10+3N$ unknowns (including instrument parameters). Every measurement results in five measured values of magnetic and gravity components along the corresponding axes. Thus, for N measurements, we obtain $5N$ readings. For $N = 5$ the problem is closed, for $N > 5$ measurements, the problem is overdetermined, and the solution can be optimized by a least-squares optimization procedure, yielding both ten instrument parameters and $3N$ orientation parameters of best fit. In detail, we need to minimize the sum

$$\sum_{j=1}^{N} \sum_{i=1}^{5} \left(S_i - a_i R_i(\phi_j) - b_i \right)^2, \tag{2}$$

where ϕ_j is the set of orientation parameters at measurement j, and $R_i(\phi_j)$ are the normalized fields projected to the instrument's coordinate system. The minimization with respect to ϕ_j, a_i and b_i is best done using the Gauss–Newton algorithm (e.g. Björk, 1996).

The calibration was done in several steps. First, a laboratory calibration measurement was used to determine the four gravimeter parameters. Once the instrument was at the field site, measurements close to the borehole were carried out to calibrate the magnetic sensors. The data processing of the sensors in the boreholes can be done using the same optimization procedure as for the calibration with the instrument parameters from the calibration kept constant and optimizing only the orientation parameters. This allows us to calculate for every measurement an orthogonal matrix, $\boldsymbol{Q}$, that describes the orientation of the instrument with respect to a reference frame fixed in space, given by the gravity and geomagnetic fields. $\boldsymbol{Q}$ contains as rows three unit vectors each describing the orientation of one of three axes of the instrument with respect to the external reference frame. The angles θ and ϕ, that are used in the next sections, are the zenith (i.e. tilt from vertical) and azimuth angles of the row of $\boldsymbol{Q}$ which corresponds to the longitudinal axis of the instrument. It would be desirable to do a similar time-series analysis for the whole orthogonal system; however, it is not yet clear how similar theoretical evolution curves for the whole system can be obtained. Details of the underlying mathematics are given in Appendix A.

MATHEMATICAL THEORY

A thin cylindrical probe inserted in the ice is assumed to move in the same way as a unit vector given by the direction of the image of a Lagrangian coordinate increment with respect to deformation. Using the notation of Hutter (1983), we denote by $\mathrm{d}X_A$ a vector increment in the reference (Lagrangian) configuration, and by $\mathrm{d}x_i(X_A)$ the corresponding vector in the present (Eulerian) configuration. Using the Einstein summation convention, we define the unit vector through its components, e_i, as

$$e_i = \frac{\mathrm{d}x_i}{\sqrt{\mathrm{d}x_j \mathrm{d}x_j}}, \tag{3}$$

so it points in the direction of the vectorial quantity $\mathbf{dx}$. The temporal evolution of the unit vector is given by

$$\dot{e}_i = L_{ij} e_j - e_i \left(e_j L_{jk} e_k \right), \tag{4}$$

where

$$L_{ij} = \frac{\partial v_i}{\partial x_j} \tag{5}$$

denotes the components of the velocity gradient. That is, the evolution of e_i is given by the projection of $L_{ij} e_j$ on a plane perpendicular to the vector e_i. A detailed derivation of Eqn (4) is given in Appendix B.

For practical purposes, we assume Cartesian coordinates with the base unit vectors $\mathbf{n}_1$, $\mathbf{n}_2$ and $\mathbf{n}_3$, such that the unit vector $\mathbf{e} = e_1 \mathbf{n}_1 + e_2 \mathbf{n}_2 + e_3 \mathbf{n}_3$. Furthermore, we use spherical coordinates with $0 \leq \theta < \pi$, $0 \leq \phi < 2\pi$ such that

$$\mathbf{e} = \begin{pmatrix} \sin\theta \cos\phi \\ \sin\theta \sin\phi \\ \cos\theta \end{pmatrix}. \tag{6}$$

Thus, the time derivative of the unit vector, $\dot{\mathbf{e}}$, has the form

$$\dot{\mathbf{e}} = \dot{\theta}\, \mathbf{a} + \dot{\phi}\, \mathbf{b}, \tag{7}$$

where the vectors

$$\mathbf{a} = \frac{\partial \mathbf{e}}{\partial \theta}, \quad \mathbf{b} = \frac{\partial \mathbf{e}}{\partial \phi}, \tag{8}$$

are orthogonal to vector $\mathbf{e}$ and orthogonal to each other,

$$\mathbf{a} \cdot \mathbf{e} = \mathbf{b} \cdot \mathbf{e} = \mathbf{a} \cdot \mathbf{b} = 0, \quad \mathbf{a} \cdot \mathbf{a} = 1, \quad \mathbf{b} \cdot \mathbf{b} = \sin^2\theta. \tag{9}$$

Scalar multiplication of Eqn (4) with $\mathbf{a}$ and $\mathbf{b}$, respectively, yields

$$a_i L_{ij} e_j = \dot{\theta} \tag{10}$$

https://doi.org/10.3189/2012JoG11J234 Published online by Cambridge University Press

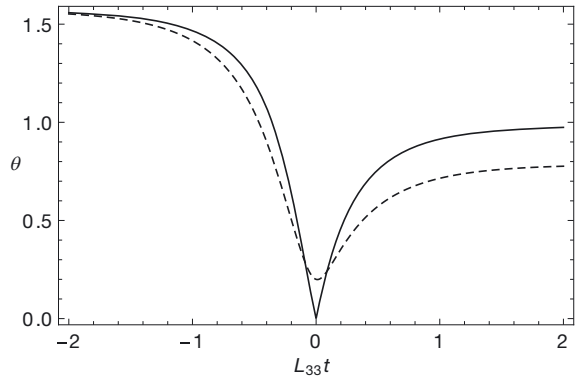

Fig. 1. Examples of possible tilt evolutions according to Eqn (15). Solid curve: $L_{13} = 3L_{33}$, $\theta_0 = 0$. Dashed curve: $L_{13} = 2L_{33}$, $\theta_0 = 0.2$, $\phi_0 = \pi/2$.

and

$$b_i L_{ij} e_j = \dot{\phi} \sin^2 \theta \ . \tag{11}$$

The second part on the right-hand side of Eqn (4), $e_i \left(e_j L_{jk} e_k\right)$, does not have any influence on $\dot{\theta}$ and $\dot{\phi}$, as it is colinear with **e**, and thus orthogonal to both vectors **a** and **b**. Equations (10) and (11) are two linear equations for the nine components L_{ij} of the velocity gradient.

The analytical solution can be used for a regression with the measured time series of zenith angles. Interestingly, the azimuth angle does not occur in the solution for θ, except for its initial value, ϕ_0, which can be used as a fitting parameter in the regression.

In principle it is possible to give an analytical solution including $L_{12} \neq 0$ as well but this is much more complicated than Eqn (16), which makes it much less useful for purposes of field data analysis.

ANALYSIS OF TIME SERIES

One absolute mono-axial (linear) inclinometer/magnetometer yields one value for $\dot{\theta}$ and $\dot{\phi}$ at one time, and thus only two equations for the nine unknowns, L_{ij}. Three linear independent unit vectors, $\mathbf{e}_k$, $k = 1, 2, 3$ with measured angles θ_k and ϕ_k yield six equations. One additional spherical inclinometer/magnetometer, tracking the rigid rotation of the velocity field, would yield three more equations, and would thus allow one to close the system of equations.

However, in many situations interesting for glaciologists, fewer than nine components L_{ij} are of interest. A suite of assumptions and approximations may reduce the number of unknowns. Some assumptions may not be trivial, though, and require careful testing to estimate the possibly imposed errors.

For a typical channel-like valley glacier it is reasonable to assume that in a coordinate system with x_1-direction along the flow and x_3 vertically (parallel to gravity), the transversal velocity component and its derivatives are comparably small, thus

$$L_{21} = L_{22} = L_{23} \approx 0. \tag{12}$$

Along a central flowline, where the transverse velocity vanishes and the along-flow velocity reaches its transversal maximum, the derivatives with respect to x_2 become small. Thus, the first-order plane-strain approximation for incompressible ice, $L_{33} = -L_{11}$, with the only non-vanishing components L_{13} and L_{33} reduces Eqns (10) and (11) to

$$\dot{\theta} = -L_{33} \left(1 + \cos^2 \phi\right) \cos\theta \sin\theta + L_{13} \cos\phi \cos^2 \theta, \tag{13}$$

$$\dot{\phi} = L_{33} \cos\phi \sin\phi - L_{13} \cot\theta \sin\phi. \tag{14}$$

In principle, Eqns (13) and (14) are linear equations for L_{13} and L_{33}, and thus could be used to calculate the temporal evolution of the velocity-gradient components. The analysis depends on the calculation of time derivatives of the measured angles, θ and ϕ. Depending on how noisy the data are, this procedure is more or less unstable and requires a smoothing of the data. Even then, the evaluation of Eqns (13) and (14) resulted in temporally drifting values for L_{13} and L_{33}, that should result in a temporal drift of the surface velocity, which could not be observed. Apart from that, L_{13} and L_{33} depend explicitly on the evolution of ϕ. The measurement of this angle requires the use of magnetometers, which are much more susceptible to environmental perturbations and thus are less accurate than gravity-based inclinometry. Furthermore, Eqns (13) and (14) are only valid in a coordinate system with the x_1-axis oriented parallel to the flow direction. The azimuth angle measured by an instrument fixed to the ice is difficult to orient absolutely in space, and thus to align with respect to the ice flow direction.

With the assumption that L_{13} and L_{33} are constant over the period considered, Eqns (13) and (14) can be solved analytically for the time evolution of the zenith angle, $\theta = \theta(t)$,

$$\theta(t) = \arctan \sqrt{\zeta(t)}, \tag{15}$$

with

$$\zeta = \mathrm{e}^{-2tL_{33}} \left(\frac{L_{13}}{L_{33}} \tan\theta_0 \cos\phi_0 - \frac{{L_{13}}^2}{2{L_{33}}^2} + \tan^2\theta_0 \sin^2\phi_0\right) + \mathrm{e}^{-4tL_{33}} \left(\tan\theta_0 \cos\phi_0 - \frac{L_{13}}{2L_{33}}\right)^2 + \frac{{L_{13}}^2}{4{L_{33}}^2}. \tag{16}$$

A detailed derivation of Eqns (15) and (16) is given in Appendix C. A numerical evaluation of this equation reproduces the same curves as the Euler scheme used by Gudmundsson and others (1999) to a high accuracy (not shown here in detail).

In Figure 1, two examples for possible tilt curves according to solution Eqn (15) are given. There are always two asymptotic values, $\pi/2$ for $L_{33}t < 0$, and

$$\theta_\infty = \arctan\left(\frac{L_{13}}{2L_{33}}\right) \tag{17}$$

on the half-axis with $L_{33}t > 0$. Thus, if the motion is dominated by shear, $L_{13} \gg L_{13}$, both asymptotes are close to $\pi/2$, whereas for $L_{13} \approx L_{33}$ significantly lower asymptotes are possible. If $\phi_0 = 0$ or $\phi_0 = \pi$ (depending on the sign of L_{33}) or $\theta_0 = 0$, the tilt reaches a minimum of $\theta = 0$ and has a kink at the minimum (solid line in Fig. 1). In all other cases the minimum is greater than zero and is passed smoothly; in these cases **e** never reaches a vertical position.

RESULTS

Field observations

Here we demonstrate the application of Eqns (15) and (16) to fit tilt data from field experiments. We consider field data from Rhonegletscher and Gornergletscher, both situated in

https://doi.org/10.3189/2012JoG11J234 Published online by Cambridge University Press

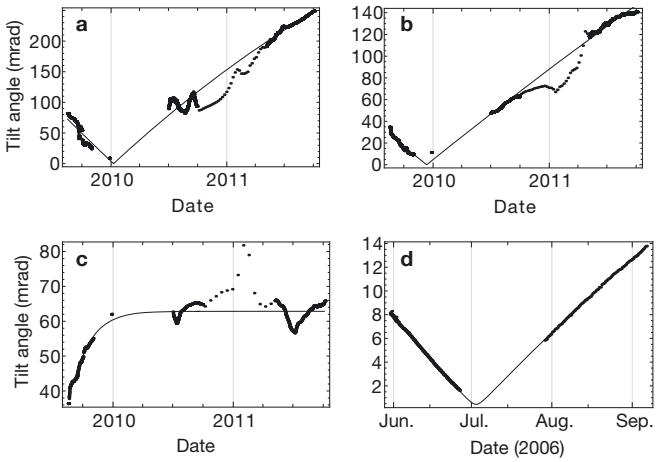

Fig. 2. Evolution of tilt angle, θ, on Rhonegletscher and Gornergletscher. The thin lines are the fitted curves according to Eqns (15) and (16). (a) Rhonegletscher, sensor B, $L_{13} = 5.55 \times 10^{-9}\,\mathrm{s}^{-1}$, $L_{33} = 3.40 \times 10^{-9}\,\mathrm{s}^{-1}$. (b) Rhonegletscher, sensor C, $L_{13} = 2.73 \times 10^{-9}\,\mathrm{s}^{-1}$, $L_{33} = 8.18 \times 10^{-10}\,\mathrm{s}^{-1}$. (c) Rhonegletscher, sensor D, $L_{13} = 1.39 \times 10^{-8}\,\mathrm{s}^{-1}$, $L_{33} = 1.10 \times 10^{-7}\,\mathrm{s}^{-1}$. (d) Gornergletscher, sensor G1, $L_{13} = 2.69 \times 10^{-9}\,\mathrm{s}^{-1}$, $L_{33} = 1.86 \times 10^{-9}\,\mathrm{s}^{-1}$.

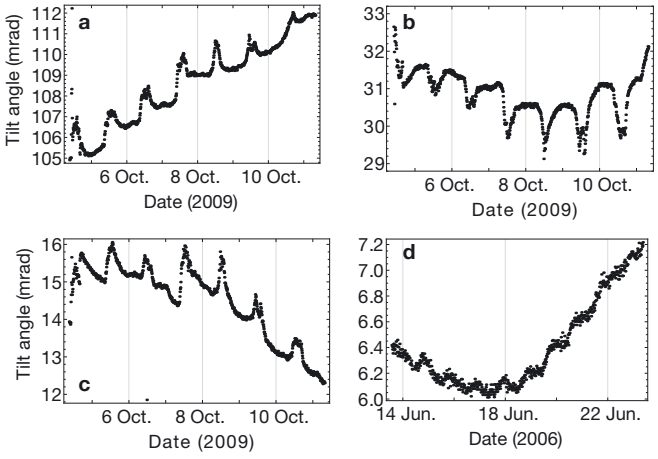

Fig. 3. Diurnal variations of tilt angles, θ, on Rhonegletscher and Gornergletscher. The scatter of the single points indicates the angular resolution of the sensor around 0.1 mrad. (a) Rhonegletscher, sensor A. (b) Rhonegletscher, sensor B. (c) Rhonegletscher, sensor C. (d) Gornergletscher, sensor G2.

the Swiss Alps. The Rhonegletscher data stem from a chain of five inclinometer/magnetometer probes that was installed in a borehole in summer 2009. The data were read every 5 min, except during winter 2010/11, when the measurement interval was extended to 8 hours in order to cope with power supply problems. The instruments are labeled A, B, C, D and E, with corresponding approximate positions of 4, 23, 40, 58 and 75 m above the glacier bed (ice thickness 119 m). The borehole is situated in temperate ice, and was permanently water-filled during the experiment. The data measured by sensor E are extremely noisy, probably due to bad coupling of the sensor to the ice. Due to large shear rates, sensor A ran out of the measurement range of the instrument within 1 year. For comparison, we also show measurements obtained with the same type of instrument installed in summer 2006 in a borehole in Gornergletscher. Instrument G1 is located 127 m above the bed (ice thickness 271 m) in cold ice of -1°C above a basal temperate layer of $\sim$70 m thickness, and can be assumed to be coupled tightly to the ice. Instrument G2 was inserted at 38 m above the bed in the temperate ice. In Figure 2 the measured tilt evolutions are displayed together with least-square fits obtained with Eqns (15) and (16).

Daily variations

At some times, the long-term evolution of the zenith angles is modulated by daily variations. These short-term variations cannot be captured by analytical tilt curves that are optimized for long periods of measurements with constant strain rates. The lowest (sensor A) and the second lowest (sensor B) instruments (Fig. 3a and b) show variations in shear strain in phase, whereas for the next highest instrument (sensor C) they are in antiphase (Fig. 3c). Interestingly, the shear rates change sign during one cycle. These variations may be caused by variations in basal sliding; however, due to possibly insufficient coupling of the instruments to the ice in the open and partially water-filled borehole, an influence of the daily variation in the water flux through the borehole cannot be excluded. Further interpretation of these patterns lies beyond the scope of this paper. Figure 3d demonstrates an example for diurnal variations in the tilt evolution inside a temperate basal layer in Gornergletscher.

CONCLUSIONS AND PROSPECTS

The analysis of the tilt evolution observed with the inclinometer/magnetometer probes is based on the assumption that a thin cylindrical probe inserted into glacier ice follows the same movement as a unit vector, which is given as the direction of the image of a Lagrangian coordinate increment with respect to deformation. The time-evolution equation for this unit vector is defined by the flow field, or more precisely, by its spatial derivatives. For simple flow fields (simple shear with some vertical and horizontal stretching), explicit analytical solutions to the evolution equations in polar coordinates were used to fit field data.

The above findings allow us to calculate theoretical tilt curves, which should be recorded by an instrument sensitive to inclination that is fixed within the material, and can therefore be helpful for calibration/validation purposes or for the reconstruction of a local flow field from tilt measurements. Of course, one could try to avoid the mathematical difficulties of solving the evolution equations analytically and just rely on a numerical integration of the coupled system. The analytical solution has, however, the great advantage that we can write down the evolution of the tilt angle, θ, without simultaneously solving the equation for the azimuth angle; instead, the evolution of θ is parameterized by the initial azimuth angle, ϕ_0.

The explicit time evolution, $\theta(t)$, has been used to fit data from inclinometer tilt experiments on Rhonegletscher and Gornergletscher, showing its ability to reproduce the measured curves. With the assumption of incompressible ice flow and the first-order plane-strain approximation, strain-rate measurements can be performed with much simpler instruments, only measuring the zenith angle of the probe axis.

Tilt measurements with high temporal resolution show examples of diurnal variations of strain rates. This phenomenon has been observed in different glaciers, such as the

https://doi.org/10.3189/2012JoG11J234 Published online by Cambridge University Press

entirely temperate Rhonegletscher, the polythermal Gornergletscher and in the polythermal region of Jakobhavns Isbræ, Greenland ice sheet (Lüthi and others, 2002). Amundson and others (2006) measured similar features on Black Rapids Glacier, a large surge-type glacier in the central Alaska Range, USA. In these examples, the patterns in variations are similar in shape and magnitude. The mechanism causing these variations and the temporal coincidence with diurnal variations in englacial water pressure suggest that variations in sliding may explain the variations in the strain field. The partial reversibility of deformations perhaps indicates diurnal variations of normal strain (Gudmundsson, 2002) or elastic reactions of the ice base to variable basal water pressure (Sugiyama and others, 2007).

An unsolved question concerns the time evolution of an orthogonal system of unit vectors fixed to a rigid body inside the material. If all unit vectors evolve as described above, the orthonormality condition may be violated in the presence of a shear motion. One therefore has to define a way to couple the rigid body to the deforming material such that orthonormality of the coordinate system fixed to it is kept. This problem can probably be addressed by modeling the motion of a rigid or hard elastic body in a deforming viscous fluid, which, however, lies beyond the scope of this paper.

One suggestion that can be drawn from the above considerations is a possible in situ measurement of the local viscosity of glacier ice. A system of three thin cylindrical inclinometer/magnetometer probes with independent orientations and the same type probe with spherical shape to measure the rigid rotation components, allows us to close the system of equations for the nine velocity-gradient components. Combined with a probe with adequate pressure sensors to measure the stress components as suggested by Pfeffer and others (2000), this yields, in principle, the complete information to compute the ice viscosity.

ACKNOWLEDGEMENTS

This work was funded by the Swiss National Science Foundation, grant No. 20021-119781/1. We thank Claudia Ryser, Martin Lüthi, Martin Funk, Jason Amundson and an anonymous reviewer for constructive input that helped improve the manuscript.

REFERENCES

Amundson JM, Truffer M and Lüthi MP (2006) Time-dependent basal stress conditions beneath Black Rapids Glacier, Alaska, USA, inferred from measurements of ice deformation and surface motion. *J. Glaciol.*, **52**(178), 347–357 (doi: 10.3189/172756506781828593)

Björk A (1996) *Numerical methods for least squares problems*. Society for Industrial and Applied Mathematics, Philadelphia, PA

Blatter H (1995) Velocity and stress fields in grounded glaciers: a simple algorithm for including deviatoric stress gradients. *J. Glaciol.*, **41**(138), 333–344

Borodulin VI, Rogalyov RN and Slabospitsky SR (1995) *CORE 2.1 (COmpendium of RElations, Version 2.1)*. ARVIX High Energy Physics, hep-ph/9507456

Copland L, Harbor J, Minner M and Sharp M (1997) The use of borehole inclinometry in determining basal sliding and internal deformation at Haut Glacier d'Arolla, Switzerland. *Ann. Glaciol.*, **24**, 331–337

Gerrard JAF, Perutz MF and Roch A (1952) Measurement of the velocity distribution along a vertical line through a glacier. *Proc. R. Soc. London, Ser. A*, **213**(1115), 546–558

Gudmundsson GH (2002) Observations of a reversal in vertical and horizontal strain-rate regime during a motion event on Unteraargletscher, Bernese Alps, Switzerland. *J. Glaciol.*, **48**(163), 566–574 (doi: 10.3189/172756502781831043)

Gudmundsson GH, Bauder A, Lüthi M, Fischer UH and Funk M (1999) Estimating rates of basal motion and internal ice deformation from continuous tilt measurements. *Ann. Glaciol.*, **28**, 247–252 (doi: 10.3189/172756499781821751)

Harper JT, Humphrey NF and Pfeffer WT (1998) Three-dimensional deformation measured in an Alaskan glacier. *Science*, **281**(5381), 1340–1342

Harper JT, Humphrey NF, Pfeffer WT, Huzurbazar S, Bahr DB and Welch BC (2001) Spatial variability in the flow of a valley glacier: deformation of a large array of boreholes. *J. Geophys. Res.*, **106**(B5), 8547–8562

Hawley RL, Waddington ED, Morse DL, Dunbar NW and Zielinski GA (2002) Dating firn cores by vertical strain measurements. *J. Glaciol.*, **48**(162), 401–406 (doi: 10.3189/172756502781831250)

Hooke RLeB and Hanson B (1986) Borehole deformation experiments, Barnes Ice Cap, Canada. *Cold Reg. Sci. Technol.*, **12**(3), 261–276

Hooke RLeB, Holmlund P and Iverson NR (1987) Extrusion flow demonstrated by bore-hole deformation measurements over a riegel, Storglaciären, Sweden. *J. Glaciol.*, **33**(113), 72–78

Hooke RLeB, Pohjola VA, Jansson P and Kohler J (1992) Intra-seasonal changes in deformation profiles revealed by borehole studies, Storglaciären, Sweden. *J. Glaciol.*, **38**(130), 348–358

Hutter K (1983) *Theoretical glaciology; material science of ice and the mechanics of glaciers and ice sheets*. D Reidel, Dordrecht/Terra Scientific, Tokyo

Lüthi M, Funk M, Iken A, Gogineni S and Truffer M (2002) Mechanisms of fast flow in Jakobshavn Isbræ, West Greenland. Part III. Measurements of ice deformation, temperature and cross-borehole conductivity in boreholes to the bedrock. *J. Glaciol.*, **48**(162), 369–385 (doi: 10.3189/172756502781831322)

Marshall HP, Harper JT, Pfeffer WT and Humphrey NF (2002) Depth-varying constitutive properties observed in an isothermal glacier. *Geophys. Res. Lett.*, **29**(23), 61 (doi: 10.1029/2002GL015412)

Moore PL, Iverson NR, Brugger KA, Cohen D, Hooyer TS and Jansson P (2011) Effect of a cold margin on ice flow at the terminus of Storglaciären, Sweden: implications for sediment transport. *J. Glaciol.*, **57**(201), 77–87 (doi: 10.3189/002214311795306583)

Paterson WSB (1976) Vertical strain-rate measurements in an Arctic ice cap and deductions from them. *J. Glaciol.*, **17**(75), 3–12

Pfeffer WT, Humphrey NF, Amadei B, Harper J and Wegmann J (2000) In situ stress tensor measured in an Alaskan glacier. *Ann. Glaciol.*, **31**, 229–235 (doi: 10.3189/172756400781820354)

Raymond CF (1971) Determination of the three-dimensional velocity field in a glacier. *J. Glaciol.*, **10**(58), 39–53

Raymond CF, Rogers JC, Taylor PL and Koci B (1994) Vertical strain measurement in core holes. *Mem. Natl Inst. Polar Res.*, Special Issue 49, 234–240

Schwerzmann A, Funk M and Blatter H (2006) Borehole logging with an eight arm caliper–inclinometer probe. *J. Glaciol.*, **52**(178), 381–388 (doi: 10.3189/172756506781828520)

Sharp RP (1953) Deformation of a vertical bore hole in a piedmont glacier. *J. Glaciol.*, **2**(13), 182–184

Shreve RL and Sharp RP (1970) Internal deformation and thermal anomalies in lower Blue Glacier, Mount Olympus, Washington, USA. *J. Glaciol.*, **9**(55), 65–86

Stuelpnagel J (1964) On the parametrization of the three-dimensional rotation group. *SIAM Rev.*, **6**(4), 422–430

Sugiyama S and Gudmundsson GH (2003) Diurnal variations in vertical strain observed in a temperate valley glacier. *Geophys. Res. Lett.*, **30**(2), 1090 (doi: 10.1029/2002GL016160)

Sugiyama S, Bauder A, Weiss P and Funk M (2007) Reversal of ice motion during the outburst of a glacier-dammed lake on Gornergletscher, Switzerland. *J. Glaciol.*, **53**(181), 172–180 (doi: 10.3189/172756507782202847)

APPENDIX A: PARAMETERIZATION OF SO(3)

To describe the orientation of three linearly independent orthogonal vectors fixed to the probe with respect to a given coordinate system, a parameterization of the group of pure rotations in three dimensions, called the special orthogonal group in three dimensions, SO(3), can be applied. Although there is no global parameterization of this group (Stuelpnagel, 1964), parameterizations of the whole group up to a finite number of singular points can be found, which is sufficient for our purpose. There are various ways to do this, such as with Euler angles. We use a matrix exponential representation of the group of special unitary transformations in two dimensions, SU(2), with Pauli matrices as generators, together with a homomorphism mapping SU(2) onto SO(3). This turned out to be computationally more convenient than using Euler angles. Independent of the parameterization, there are always three independent parameters describing the orientation of the instrument, reflecting the dimension of the group SO(3).

For every set of group parameters, we generate a unitary matrix, $\boldsymbol{U} \in \mathrm{SU}(2)$, by the usual exponential representation with Pauli matrices as generators. Then, we calculate the corresponding orthogonal matrix, $\boldsymbol{O} \in \mathrm{SO}(3)$, by

$$O^{ij}[\boldsymbol{U}] = \frac{1}{2}\mathrm{Tr}\left[\tau^i \boldsymbol{U} \tau^k \boldsymbol{U}^\dagger\right], \tag{A1}$$

where τ^i, $i \in \{1,2,3\}$ are Pauli matrices and $\boldsymbol{U}^\dagger$ denotes the Hermitian adjoint of $\boldsymbol{U}$. Using the Fierz identity (Borodulin and others, 1995),

$$\tau^i_{AB}\ \tau^i_{CD} = 2\delta_{AD}\ \delta_{BC} - \delta_{AB}\ \delta_{CD}, \tag{A2}$$

both the orthogonality of $\boldsymbol{O}$,

$$O^{ik}O^{jk} = \delta^{ij}, \tag{A3}$$

and the homomorphism property

$$O^{ik}[\boldsymbol{U}]O^{kj}[\boldsymbol{V}] = O^{ij}[\boldsymbol{U}\boldsymbol{V}] \quad \forall\ \boldsymbol{U}, \boldsymbol{V} \in \mathrm{SU}(2) \tag{A4}$$

can be proved.

APPENDIX B: TIME DERIVATIVE OF UNIT VECTOR

The mapping of Lagrangian onto Eulerian coordinates (i.e. the time evolution of the material) yields

$$e_i = \frac{F_{iA}\mathrm{d}X_A}{\sqrt{F_{jB}F_{jC}\mathrm{d}X_B\mathrm{d}X_C}}, \tag{B1}$$

where

$$F_{iA} = \frac{\partial x_i}{\partial X_A} \tag{B2}$$

is the deformation gradient. The time evolution of $\boldsymbol{e}$ is given by

$$\dot{e}_i = \frac{\dot{F}_{iA}\mathrm{d}X_A}{\|\mathbf{d}\boldsymbol{x}\|} - F_{iA}\mathrm{d}X_A\frac{\left(\dot{F}_{jB}F_{kC} + F_{jB}\dot{F}_{kC}\right)\mathrm{d}X_B\mathrm{d}X_C}{2\|\mathbf{d}\boldsymbol{x}\|^3}. \tag{B3}$$

With the identity $\dot{F}_{iA} = L_{ij}F_{jA}$ (Hutter, 1983), where

$$L_{ij} = \frac{\partial v_i}{\partial x_j} \tag{B4}$$

denotes the velocity gradient, we obtain

$$\begin{aligned}\dot{e}_i &= L_{ij}e_j - e_i\frac{\left(L_{jk}F_{kB}F_{jC} + F_{jB}L_{jk}F_{kC}\right)\mathrm{d}X_B\mathrm{d}X_C}{2\|\mathbf{d}\boldsymbol{x}\|^2}\\ &= L_{ij}e_j - e_i\left(e_jL_{jk}e_k\right).\end{aligned} \tag{B5}$$

APPENDIX C: TEMPORAL EVOLUTION OF ZENITH ANGLE

Depending on the initial conditions, solving Eqns (13) and (14) may require a number of case distinctions. In order to avoid most of them we will restrict our considerations to the case that is of interest for our application: initial conditions close to vertical, i.e. $0 \le \theta_0 < \pi/2$. Now, we only have to take care if $\theta = 0$, as this is a singular point of the spherical coordinates (Eqn (6)) where the angle ϕ is not well defined. This can be the case either initially, $\theta_0 = 0$, or if $\phi_0 \in \{0, \pi\}$; we consider these cases separately below and assume at first initial values $0 < \theta_0 < \pi/2$ and $\phi_0 \notin \{0, \pi\}$. As $\theta \neq 0$, we can use the bi-unique substitutions

$$\zeta = \tan^2\theta, \quad \omega = \tan\theta\cos\phi \tag{C1}$$

in Eqns (13) and (14), yielding

$$\dot{\omega} = -2L_{33}\omega + L_{13}, \tag{C2}$$

$$\dot{\zeta} = -2L_{33}\zeta - 2L_{33}\omega^2 + 2L_{13}\omega. \tag{C3}$$

The transformation partly decouples the system. The solution for ω is

$$\omega(t) = C_1\mathrm{e}^{-2L_{33}t} + \frac{L_{13}}{2L_{33}}, \tag{C4}$$

where C_1 is an integration constant. Substituting this solution in Eqn (C3) yields

$$\dot{\zeta} = -2L_{33}\zeta - 2L_{33}C_1^2\mathrm{e}^{-4L_{33}t} + \frac{{L_{13}}^2}{2L_{33}}, \tag{C5}$$

with the solution

$$\zeta(t) = C_1^2\mathrm{e}^{-4L_{33}t} + \frac{{L_{13}}^2}{4{L_{33}}^2} + C_2\mathrm{e}^{-2L_{33}t}, \tag{C6}$$

and a second integration constant, C_2. The two integration constants can be determined from the initial conditions

$$\omega(0) = \tan\theta_0\cos\phi_0 = \alpha, \tag{C7}$$

$$\zeta(0) = \tan^2\theta_0 = \beta, \tag{C8}$$

and for $\omega(t)$ and $\zeta(t)$ we obtain

$$\omega(t) = \left(\alpha - \frac{L_{13}}{2L_{33}}\right)\mathrm{e}^{-2L_{33}t} + \frac{L_{13}}{2L_{33}}, \tag{C9}$$

$$\begin{aligned}\zeta(t) = &\left(\alpha - \frac{L_{13}}{2L_{33}}\right)^2\mathrm{e}^{-4L_{33}t} + \frac{{L_{13}}^2}{4{L_{33}}^2}\\ &+ \left(\beta - \alpha^2 + \alpha\frac{L_{13}}{L_{33}} - \frac{{L_{13}}^2}{2{L_{33}}^2}\right)\mathrm{e}^{-2L_{33}t}.\end{aligned} \tag{C10}$$

Finally, the solution for the zenith angle, θ, as a function of time is given in Eqns (15) and (16).

In the critical cases mentioned above, a critical situation only arises at the time when $\theta = 0$ is reached (before this moment, Eqns (C9) and (C10) remain valid). As the evolution

https://doi.org/10.3189/2012JoG11J234 Published online by Cambridge University Press

equations are of first order, we can simply assume that this is the case initially, and set $\theta_0 = 0$. In consequence, at $t = 0$ we may use neither the angle ϕ nor the substitutions (Eqn (C1)). However, at $t = 0$ the vector $\mathbf{e}$ is simply $\mathbf{e} = (0, 0, 1)$, and Eqn (4) yields

$$\dot{\mathbf{e}} = (L_{13}, 0, 0)\,, \tag{C11}$$

i.e. after a small time increment, Δt, we arrive at

$$\mathbf{e} = \big(L_{13}\Delta t, 0, 1\big) + \mathcal{O}(\Delta t)^2. \tag{C12}$$

This corresponds (to lowest order in Δt) to $\theta = L_{13}\Delta t$ and $\phi = 0$ or $\phi = \pi$ (depending on the sign of L_{13}), and from $t = \Delta t$ onwards we may again use Eqns (C9) and (C10) with these initial conditions. As, furthermore, in the limit $\Delta t \to 0$ we arrive at $\theta(0) = 0 = \theta_0$, we may extend the validity of Eqns (C9) and (C10) to the critical case $\theta_0 = 0$ if we use the convention to set the initial condition for the (initially undefined) azimuth angle to $\phi_0 = 0$ or $\phi_0 = \pi$ (depending on the sign of L_{13}).

MS received 15 November 2011 and accepted in revised form 2 Febuary 2012

https://doi.org/10.3189/2012JoG11J234 Published online by Cambridge University Press